Polarization-Dependent Multipolar Plasmon Resonances in Anisotropic Multiscale Au Particles

Eun-Ah You,[†] Wei Zhou,[‡] Jae Yong Suh,[†] Mark D. Huntington,[‡] and Teri W. Odom[†,‡,*]
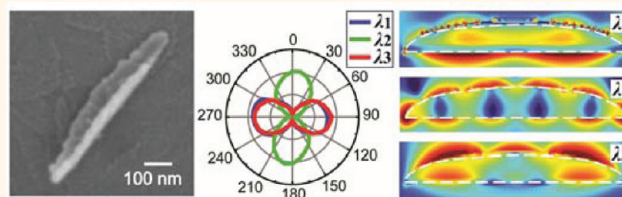
[†]Department of Chemistry, and [‡]Department of Materials Science and Engineering, Northwestern University, Evanston, Illinois 60208, United States

Localized surface plasmons (LSPs) are collective charge oscillations confined to the surface of metal nanostructures.[1] The properties of LSPs depend on the size, shape, and material of the nanoparticles (NPs) as well as the local dielectric environment.[2−5] When the dimension (d) of a metal NP is much smaller than the wavelength (λ) of the incident electromagnetic (EM) field ($d \ll \lambda$), the free electrons in the NP can oscillate with the same phase in the form of a dipole mode ($l = 1$).[6−9] In contrast, when d is comparable to or larger than λ, conduction electrons at different locations of the particle can oscillate with different phases, which results in the excitation of higher order quadrupole ($l = 2$) or multipolar modes ($l \geq 2$).[7,9−14]

Multipolar plasmon resonances are not only of fundamental interest but can also be exploited for various applications such as surface-enhanced Raman scattering,[15−17] plasmon-enhanced second harmonic generation,[18] and directional scattering.[19] Higher-order modes have been observed in large planar structures such as triangular-[13,20,21] and crescent-shaped particles[22,23] as well as in nonplanar structures including spheres,[24,25] shells,[26] rods,[11,27,28] and pyramidal shells.[5,29−31] Because of their three-dimensional (3D), anisotropic geometry, Au pyramidal shells support multipolar plasmon resonances that depend on incident angle and polarization direction of the EM field. For example, the quadrupole resonance depends on the excitation direction since this mode is spatially localized in the base plane of the pyramid.[5,29]

One distinctive characteristic of anisotropic metal NPs is their polarization-dependent optical properties. The mapping of an optical response as a function of polarization angle can be used to identify different plasmon resonances *within* a single particle, and the LSPs can be correlated to specific geometric features of the NPs.[32−34] Previous studies showed that variations in the shape of ends of rod-shaped particles could shift the peak positions of the LSPs compared to nanorods with the same lengths.[33,35] Detailed studies on how geometrical changes in 3D, anisotropic NPs correlate to optical properties have not been extensively reported because of the difficulty in controlling size and shape. Although solution syntheses can produce various NP geometries, precise control over nanoscale features is challenging.[34] In typical top-down methods, structures in 2D are possible, but 3D anisotropic particles cannot be created.[36,37] The phase-shifting photolithography, etching, e-beam, and lift-off (PEEL) procedure for fabricating pyramidal shells can, however, be used to

ABSTRACT

This paper reports the fabrication and characterization of three-dimensional (3D) multiscale Au particles with different aspect ratios. Increasing the length of the particles resulted in excitation of a longitudinal mode and two different transverse modes having different multipolar orders. The multipolar orders increased for both longitudinal and transverse modes as the aspect ratio increased. Finite-difference time-domain calculations revealed that the structural asymmetry of the 3D anisotropic particles were the reason for the two distinct transverse plasmon resonances. When the 3D structural change occurred at the ends of the multiscale particle, however, the optical response showed two resonances in the longitudinal direction and only a single resonance in the transverse direction.
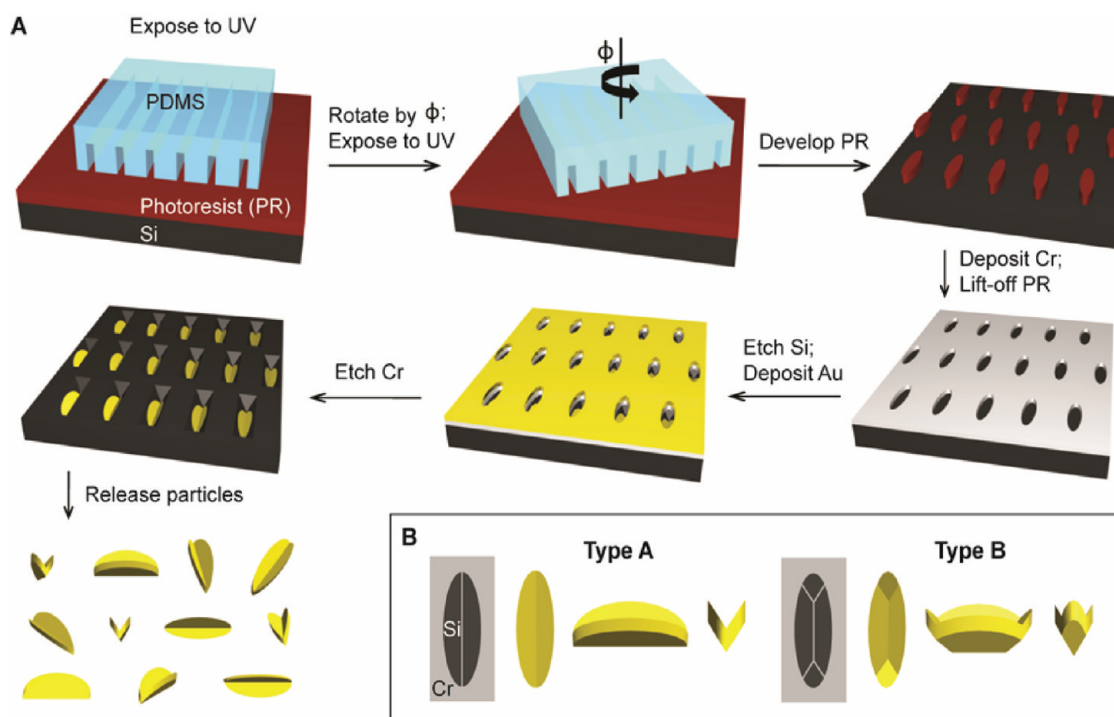
Figure 1. 3D anisotropic multiscale Au particles with different aspect ratios can be fabricated using a variation of the PEEL process. (A) Fabrication scheme for multiscale Au NPs. The ARs of multiscale particle can be altered by changing ϕ between two sequential UV exposures through a SIL line photomask. (B) The ends of type A and B particles are determined by the anisotropic etching of intersecting Si (111) faces in the Si (100) template.

generate various shapes of 3D anisotropic particles with well-defined dimensions.[31,38,39] The size and shape of the NPs can be tailored by modifying one or more of the different steps in the PEEL process including photolithography, etching, or e-beam metal deposition. Thus, fabricated NPs can serve as a platform to investigate the effects of nanoscale structural changes in multiscale particles on their optical response.

In this Article, we report the fabrication of 3D, multiscale Au particles with different aspect ratios (ARs) and characterization of their polarization-dependent plasmon resonances. The LSPs measured in visible and near-infrared (NIR) wavelengths were identified as multipolar plasmons, and the resonances were correlated with specific structural features of the anisotropic NPs using finite-difference time-domain (FDTD) simulations. The multiscale NPs with different ARs supported a single longitudinal plasmon resonance and two distinct transverse plasmon resonances, where multipolar orders increased for both longitudinal and transverse modes with increased AR. When a 3D structure of the ends was changed in the particle with same dimension, the LSP response was altered to support two LSPs in the longitudinal direction and a single resonance in the transverse direction.

RESULTS AND DISCUSSION

Fabrication of Multiscale Particles with Different Aspect Ratios. Anisotropic Au particles were created by modifying the "P" step in PEEL (Figure 1A). The shape of the

photoresist (PR) posts on a Si (100) wafer were changed from circular to ellipse by altering the angle (ϕ) between two sequential UV light exposures through a soft interference lithography (SIL) photomask with recessed, periodic 1D-line patterns (width, 100 nm; depth, 400 nm; pitch, 400 nm).[40] Here, ϕ was decreased from 90° to 17° to create circular and elliptical posts with ARs ranging from 1.0 to 7.7, where AR is defined as the length of the long axis of the ellipse divided by the short axis. We optimized the exposure and development conditions so that all PR patterns had nearly the same short axis length (∼120 nm). The long axis of the PR features ranged from 100 nm to >1 μm depending on ϕ.

After deposition of a thin layer of Cr and lift-off of the PR, the Si (100) substrate was anisotropically etched in a KOH/isopropyl alchohol solution.[38] The etching conditions were adjusted to create two types of particles (Figure 1B). In type A, only two intersecting Si (111) faces parallel to the long axis were exposed to metal deposition through the Cr hole; in type B, intersecting Si (111) faces were exposed resulting in a structural change at the ends of the particle. Next, 20 nm of Au was deposited on the etched Si template/ Cr hole array template. After the Cr/Au film was removed, the multiscale Au particles were released by etching the Si substrate in aqueous KOH solution. Figure 2 displays fabricated type A multiscale Au particles with different ARs ranging from 1.0 to 7.7.

Optical Response of Multiscale Particles with Different Aspect Ratios. To investigate the effect of length on the optical
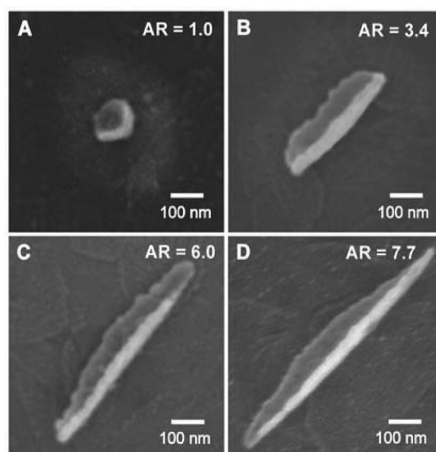
Figure 2. Multiscale Au particles with different aspect ratios. Scanning electron microscopy (SEM) images of the particles with ARs of (A) 1.0, (B) 3.4, (C) 6.0, and (D) 7.7. ϕ was 90°, 28°, 20°, and 17° for AR = 1.0, 3.4, 6.0 and 7.7, respectively. The AR = 1.0 particle is a pyramidal shell, and the particles with AR = 3.4−7.7 have the straight ends (type A).

properties of multiscale particles, we measured the polarization-dependent scattering from type A particles with different ARs. Single particle, dark field (DF) scattering of Au particles with AR of 3.4, 6.0, and 7.7 were measured at polarization angles (α) from 0° to 360° in 10° steps (α: angle between the polarization direction of excitation light and the long axis of particle). Note that the lengths of the type A NPs (380, 698, and 1012 nm for AR 3.4, 6.0, and 7.7, respectively) were different by at least 300 nm in order to evaluate the effects of length close to the incident wavelength of light. The multiscale particles showed multiple peaks at measured visible and NIR wavelengths (420−980 nm). Using a Lorentzian multipeak fitting algorithm,[23,41,42] we separated the overlapped scattering peaks into individual resonances. Figure 3 shows three resolved resonances from the overlapped multiple peaks measured under transverse polarization (α = 90°) for particles with different ARs. The multipeak analysis using a Lorentzian fit was used for all the scattering spectra measured from α = 0° to 360°. The scattering spectra measured under longitudinal polarization (α = 0°) in Supporting Information, Figure S1 also shows how the different spectral profile can be resolved into individual resonances. Three peaks based on the fits for each particle were analyzed and assigned λ_1, λ_2, and λ_3. The peak positions (λ_1, λ_2, λ_3) were 638, 726, and 832 nm for AR = 3.4; 657, 804, and 891 nm for AR = 6.0; and 676, 767, and 867 nm for AR = 7.7.

To show the polarization-dependent response of each resolved LSP, the scattering intensities of the resolved plasmon resonances were displayed in a polar plot (Figure 4). Instead of plotting absolute intensities, we plotted the relative values as a function of α while setting the minimum values close to zero in the polar
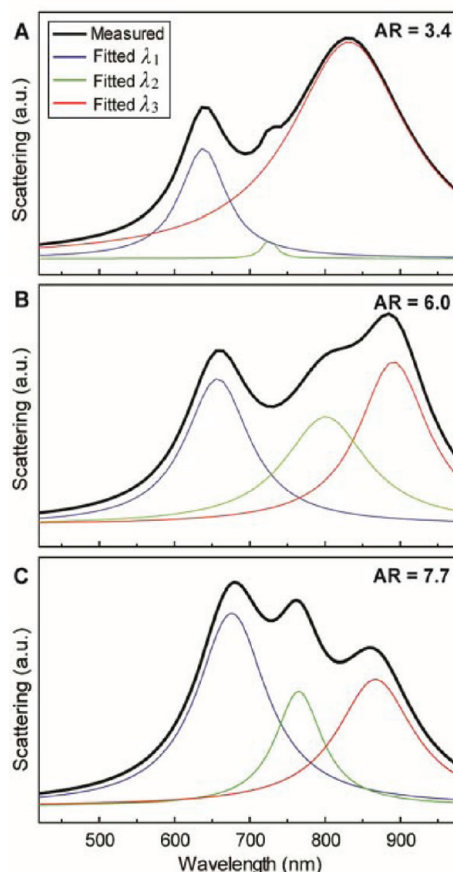

Figure 3. Multiple peak analysis of single particle scattering in multiscale Au particles. The overlapped, three LSPs from particles with AR of (A) 3.4, (B) 6.0, and (C) 7.7 can be resolved into individual resonances using a multipeak Lorentzian fit. Although the measured spectra at the polarization angle, α = 90° are presented here, the same analysis using Lorentzian multipeak fitting was used for all measured scattering data from α = 0° to 360°.

plots. The relative values enabled variations in the scattering intensity to be displayed more clearly for comparison. For the particles with different ARs, the scattering intensities of λ_1 and λ_3 were maximized when the incident polarization was *perpendicular* to the long axis of the particle (α = 90°). In contrast, the scattering intensity at λ_2 was highest when the incident polarization was *parallel* to the long axis of the particle (α = 0°). The relative scattering intensities of λ_1, λ_2, and λ_3, however, were different for particles with different ARs. We found that independent of AR, all particles supported three distinct LSP modes with different relative scattering intensities. One mode is maximized along the long axis of the particle, and the other two along the short axis. These polarization-dependent responses are distinct because three different modes in multiscale particles can be excited under longitudinal and transverse polarizations. In contrast, fabricated nanorods only show two modes with polarization effects, one that exhibits a strong polarization response along the long axis, and the
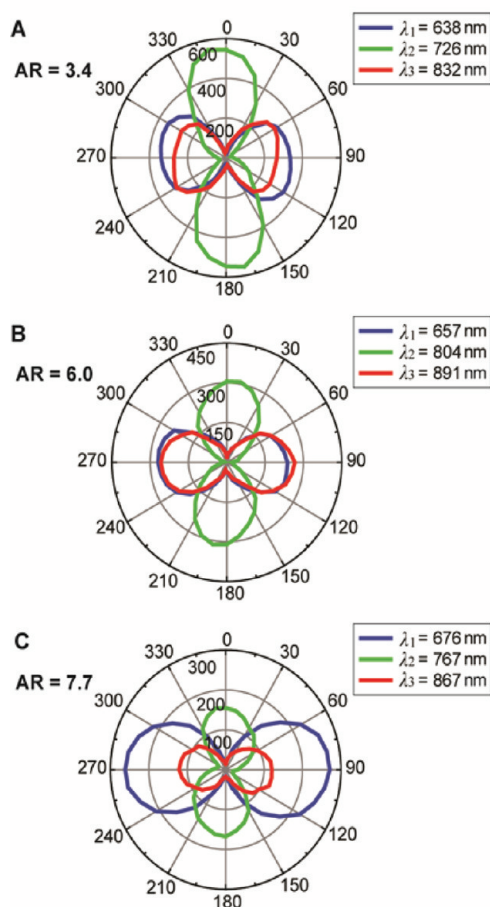
Figure 4. Polarization-dependent optical responses in multi-scale particles with various ARs. Polar plots show the relative scattering intensities of three resolved resonances as a function of polarization angle for the particle with AR of (A) 3.4, (B) 6.0, and (C) 7.7. Particles with different ARs showed the same trends in the polarization-dependent responses. λ_2 shows a maximum intensity along the long axis of the NPs, and λ_1 and λ_3 exhibit the highest intensities along the short axis of the NPs.

other that shows very weak polarization response along the short axis of nanorods.[33,43]

FDTD Calculations of Plasmon Resonances. FDTD methods[44−47] were used to calculate the single particle scattering spectra, the distribution maps of the electric field intensity ($|\mathbf{E}|^2$) and the real part of electric field (Re($\mathbf{E}$)) at λ_1, λ_2, and λ_3. To simulate the experimental conditions of light incident on a single particle, we selected different wavevectors **k** at every 45° relative to the optical axis to cover the major directions of light from a DF condenser for the scattering spectra calculations. The incident excitation angle (θ) was taken as the average value of the numerical aperture used in the experiment (0.80−0.95) with the refractive index of the immersion oil = 1.525. The calculations showed that two excitation directions directed at the middle of the particle ($\theta = 37°$ and $−37°$) resulted in dominant contributions to the measured scattering properties
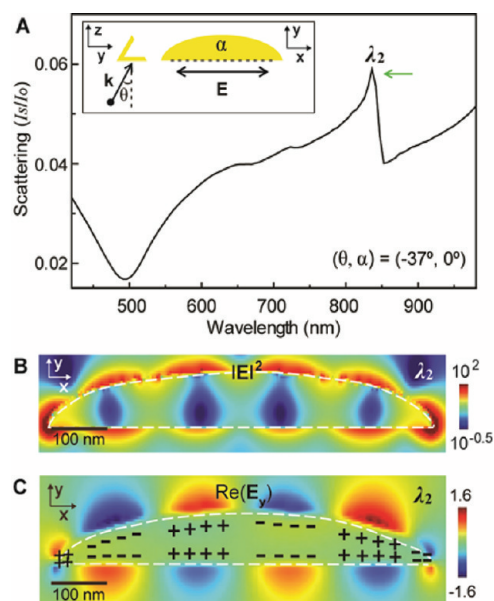

Figure 5. Multipolar longitudinal mode at λ_2 in the AR 6.0 particle. (A) The calculated single particle scattering spectra excited at $(\theta, \alpha) = (−37°, 0°)$. (B) $|\mathbf{E}|^2$ shows five nodes along the long axis of the particle ($l = 5$). (C) Re(E_y) distribution exhibits a longitudinal charge oscillation along the long axis of the particle.

(Supporting Information, Figure S2). Thus, we investigated four excitation conditions with two polarization angles α of the incident plane wave: $(\theta, \alpha) = (−37°, 0°)$, $(37°, 0°)$, $(−37°, 90°)$ and $(37°, 90°)$. The geometry of excitation light is illustrated in the insets of Figures 5 and 6.

We compared the peak positions of the measured plasmon resonances and the calculated scattering peaks at the same representative excitation directions. The scattering spectra calculated at $(−37°, 0°)$ and $(37°, 0°)$ were compared to the measured wavelength λ_2 that was maximized under longitudinal polarization, and the scattering from $(−37°, 90°)$ and $(37°, 90°)$ conditions was compared with λ_1 and λ_3, which showed the highest intensities under transverse polarization. The resonances from simulations matched well with the measured LSPs, which we have designated λ_1, λ_2, and λ_3. The scattering spectra calculated at $(\theta, \alpha) = (−37°, 0°)$ and $(37°, 0°)$ indicate that the dipole mode exists around 1750, 3000, and 4150 nm for particles with AR 3.4, 6.0, and 7.7, respectively (Supporting Information, Figure S3). To test the validity of our analysis, we measured the extinction spectra of an array of Au particles with AR 3.4 using a UV−vis−NIR spectrophotometer (Supporting Information, Figure S4). The measured dipolar resonance was centered around 1750 nm, which matched well with the calculated scattering spectra of a single particle.

In Figure 4, the relative scattering intensities of the three LSP resonances are different for the different AR particles. For the shortest particle (AR = 3.4), the intensity of the longitudinal mode was higher than
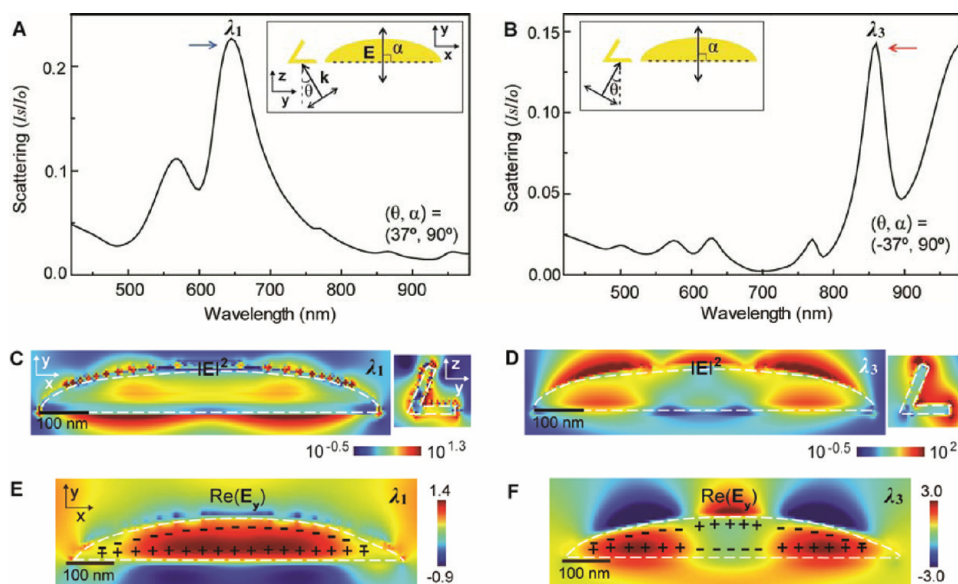
Figure 6. Two different transverse modes at λ_1 and λ_3 in the AR 6.0 particle. The calculated far-field and near-field properties reveal two distinctive transverse modes at λ_1 and λ_3. Single particle scattering spectra presenting (A) λ_1 excited at $(\theta, \alpha) =$ (37°, 90°) and (B) λ_3 at $(\theta, \alpha) = (-37°, 90°)$. The different $|E|^2$ maps in the $x-y$ plane including one face of the particle, and the $y-z$ plane including the cross-section at (C) λ_1 and (D) λ_3. Different multipolar orders and electric field intensity distributions are shown for the two transverse LSPs. Re(E$_y$) distributions show distinct transverse charge oscillations in the $x-y$ plane at (E) λ_1 and (F) λ_3.

the intensity of the LSPs along the transverse directions. As the length was increased (AR = 6.0), the relative intensities of all three modes were approximately equal. When the length was further increased (AR = 7.7), the intensity of one of the LSPs along the short axis increased, and the other resonances decreased. These differences in scattering intensities can be understood by the different scattering intensities of λ_1, λ_2, and λ_3 calculated at $(\theta, \alpha) = (37°, 90°)$, $(-37°, 0°)$ and $(-37°, 90°)$, respectively. In the calculated scattering spectra, λ_2 corresponds to a resonance excited by both $(\theta, \alpha) = (-37°, 0°)$ and $(37°, 0°)$. For the transverse modes in the single particles, the simulated scattering reveal that λ_1 and λ_3 correspond to distinct LSPs excited at $(\theta, \alpha) = (37°, 90°)$ and $(-37°, 90°)$. For particles with different ARs, the intensities vary for the three modes because (1) the intensity of higher-order modes is lower than lower-order modes[14,48] (Supporting Information, Figures S3 and S5); and (2) the multipolar orders for the respective λ_1, λ_2 and λ_3 are different for the different ARs (Supporting Information, Figure S6). The calculated spectra revealed that as the AR increased, the relative intensity of λ_3 compared to λ_1 decreased because the multipolar order of λ_3 was higher. The calculated scattering spectra are in reasonable qualitative agreement with the measured relative intensities of λ_1, λ_2, and λ_3.

Identification of Multipolar Longitudinal Modes. Because all the type A particles showed the same polarization-dependent scattering trends, we will analyze in detail only the AR 6.0-particle (Figure 5). Calculations of AR 3.4 and 7.7 particles are in the Supporting

Information. Figure 5A displays the scattering spectra for the λ_2 resonance excited at $(\theta, \alpha) = (-37°, 0°)$ for the AR 6.0 particle. The same characteristic resonance was excited by $(\theta, \alpha) = (-37°, 0°)$ and $(37°, 0°)$, which occurs at 836 nm by $(-37°, 0°)$ and 826 nm by $(37°, 0°)$. Therefore, the LSP resonance excited under longitudinal polarization is determined by the elongated structure rather than the anisotropic structure in the multiscale particle, and hence only far-field scattering and near-field electric field maps calculated at $(\theta, \alpha) = (-37°, 0°)$ are only shown.

We determined the multipolar order (*l*) of each resonance by calculating the near-field optical properties $|E|^2$ and observing the number of nodes of the standing-wave patterns in the $|E|^2$ map.[9,49,50] The direction of charge oscillations at specific resonances can be identified from Re(**E**), which displays phase differences between the electric field of the positive and negative charge density regions.[46,47] According to boundary conditions derived from Maxwell's equations, the surface charge density (σ) is related to the normal components of the electric field **E** as $(\varepsilon_2 \mathbf{E}_2 - \varepsilon_1 \mathbf{E}_1) \cdot \mathbf{n} = 4\pi\sigma$, where ε is the dielectric constant, and **n** is the unit vector normal to the interface between medium 1 and medium 2.[51] In the Re(**E**$_y$) maps, **E**$_y$ is the electric component normal to the interface defined by the particle and its dielectric environment, and so its direction and strength indicate whether charges are accumulated or depleted at different positions on the particle. In particular, the red and blue colors correspond to the positive and negative directions of **E**$_y$. The sign of the surface
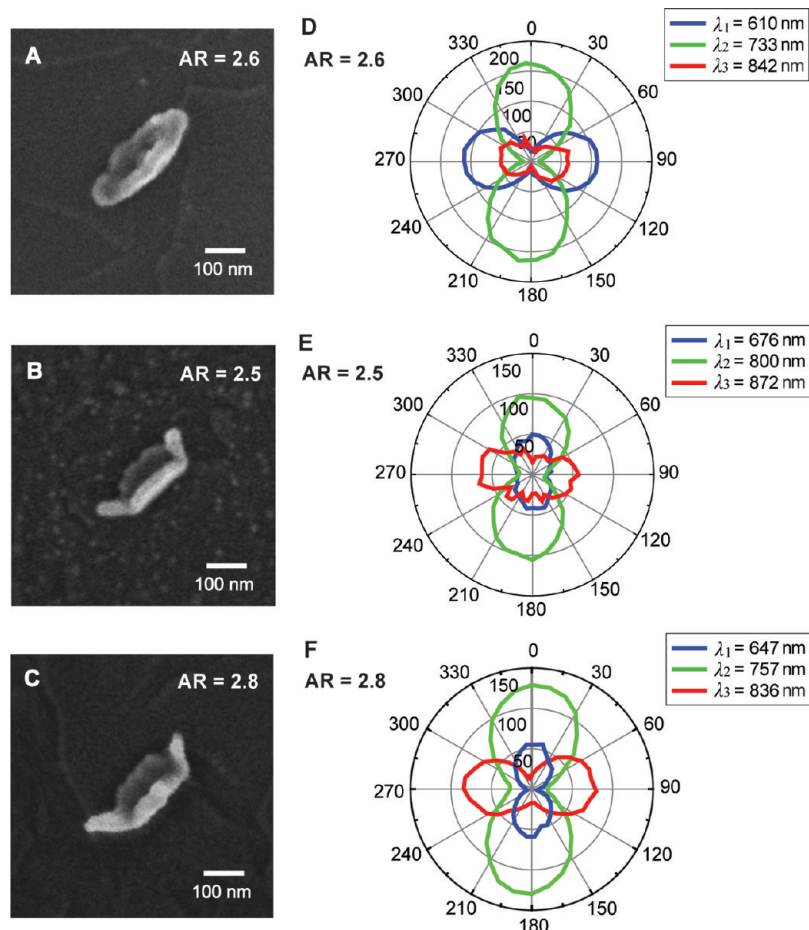
Figure 7. Different optical response of multiscale particles with 3D structural change at the ends. SEM images of (A) AR = 2.6 particle (type A), (B) AR = 2.5 particle (type B), and (C) AR = 2.8 particle (type B) support different 3D ends. The polarization-dependent responses of (D) AR = 2.6, (E) AR = 2.5, and (F) AR = 2.8 particles indicate that the AR = 2.6 particle showed the highest scattering intensity of λ_2 along the long axis and λ_1 and λ_3 along the short axis of NP while the AR = 2.5 and 2.8 particles (type B) supported the maximum intensity of λ_1 and λ_2 along the long axis and λ_3 along the short axis of the NPs.

charge density can be calculated by $\varepsilon_2\mathbf{E}_{y2} - \varepsilon_1\mathbf{E}_{y1}$, where 2 is the dielectric ($\varepsilon_2 = 2.3$) and 1 is the Au metal in our case.

Figure 5B displays the electric field intensity distribution at λ_2 in the $x–y$ plane where one face of the particle is in contact with the substrate. Since the $x–y$ plane includes an entire section of the multiscale particle, the $|\mathbf{E}|^2$ map in this plane captures the main near-field optical properties. The electric field map shows six high intensity regions across the particle, which indicates $l = 5$ for the AR 6.0-particle. Figure 5C depicts the Re($\mathbf{E}_y$) distribution at λ_2 in the $x–y$ plane. The map of the real part of the electric field exhibits a phase change between six alternating high intensity regions along the x-axis, which indicates that charges oscillate along the long axis of the particle at this resonance. In addition, the Re($\mathbf{E}_y$) map shows the same higher-order mode ($l = 5$) as the $|\mathbf{E}|^2$ map. Therefore, the near-field optical properties confirm that λ_2 is a multipolar longitudinal plasmon resonance.

As the aspect ratio of the multiscale particles increased, plasmon resonances with increased multipolar order were sustained in the same wavelength ranges (Supporting Information, Figure S6), which is consistent with previous work on other anisotropic particles.[7,9,11,48,52] The multipolar order for λ_2 was determined as $l = 3$, 5, and 7 for the AR 3.4, 6.0, and 7.7-particles from their $|\mathbf{E}|^2$ maps. Higher ARs result in a given multipolar order being shifted to longer wavelengths and an increased number of higher order modes within a fixed wavelength range, which was also observed in Au nanorods fabricated in anodized aluminum oxide templates.[11] Comparable to the dimensions of our multiscale particles (lengths of nanorods between 735 nm (AR 8.6) and 1175 nm (AR 13.8)), the two rod lengths showed $l = 5$, 7 modes around 660 nm and 650–700 nm, respectively. The multiscale particles with AR 6.0 and AR 7.7 exhibited $l = 5$ and 7 modes at 804 and 767 nm, which exist at longer wavelengths because of the tapering of the particles at their ends and because there is less overall gold material.

Different Transverse Modes in the 3D Particles. The calculated resonances at λ_1 (645 nm) and λ_3 (858 nm) in the AR 6.0 particle, which correspond to the measured λ_1 (657 nm) and λ_3 (891 nm) in the polar plots, are resonances excited by $(\theta, \alpha) = (37°, 90°)$ and $(-37°, 90°)$, respectively (Figures 6A,B). Notably, the two different excitations resulted in the distinct LSPs at λ_1 and λ_3 because of light interacting with different geometric features. These two resonances, which are separated by >200 nm in wavelength, are a direct signature of the structural asymmetry of the 3D anisotropic particle. The electric field intensity distributions at λ_1 and λ_3 also exhibit different near-field properties. $|\mathbf{E}|^2$ maps of the particle reveal different multipolar orders of λ_1 and λ_3, where λ_3 has a larger number of nodes compared to λ_1 (Figures 6C,D). λ_3 is not a higher-order mode of λ_1, however, because λ_1 and λ_3 are resonances excited by different excitation directions. Because of the 3D anisotropic structure of the multiscale particles, different $\mathbf{k}$-vectors interact with different portions of the particle, and hence distinct far-field and near-field properties can result. The multipolar orders of λ_1 and λ_3 resonances are not comparable and need to be assigned independently.

The scattering spectra and $|\mathbf{E}|^2$ maps show that the scattering intensity at λ_1 is higher than λ_3 but the electric field intensity at λ_1 is lower than λ_3 (Figures 6A-D). This result can be understood by previous calculations that indicate that the peak wavelengths of far-field resonances with their maximum intensities are different from the wavelengths of near-field resonances with their maximum intensities.[53] The near-field properties are related to the ability of the particle to convert incoming light into localized fields, while the far-field properties represent the ability of the particle to absorb light and/or convert it into a propagating wave. In the case of spherical NPs with radius r, the near-field property is dominated by a $1/r^3$ term while the far-field is dominated by $1/r$ term in Mie theory. Therefore, the maximum intensities for both near-field and far-field properties usually do not occur at the same wavelength.

For λ_1 and λ_3, the cross-section through the center of the particle shows distinct electric field distributions at the two resonances. For example, the weak field intensity at λ_1 in the cross section is distributed over the entire particle, but the high intensity field at λ_3 is concentrated at the two open edges of the particle. Also, Re($\mathbf{E}_y$) displays different transverse oscillations of charge density at λ_1 and λ_3, where the charge density waves with different numbers of nodes oscillate *perpendicular* to the long axis of the particle at the two LSPs (Figure 6E,F). Hence, λ_1 and λ_3 are different multipolar transverse modes as a result of the structural asymmetry of the 3D multiscale particle, which is a unique optical feature of multiscale particles.

Effect of 3D Structural Change on Optical Response. Besides the effects of changing the length of the 3D NPs, we studied the optical properties of multiscale particles with 3D structural changes at the ends (Figure 7A–C). For clarification, we assign multiscale particles with 3D ends as type B particles. We compared AR = 2.5 and 2.8 particles (type B) to the AR = 2.6 particle (type A), which are similar in length (<20 nm difference among particles) but with different terminal features. Similar to previous results on type A particles, the AR = 2.6 particle showed the highest scattering intensity of a single resonance (λ_2) along the long axis and two resonances (λ_1 and λ_3) along the short axis of particle (Figure 7D). In contrast, the AR = 2.5 and 2.8 particles supported two resonances (λ_1 and λ_2) that were maximized along the long axis of the particle and only a single resonance (λ_3) along the short axis (Figures 7E,F); FDTD calculated results were in agreement (Supporting Information, Figure S7). In contrast to the AR = 2.5 and 2.8 particles exhibiting strong polarization effects at three different LSP resonances, a nanopyramid showed only a very weak polarization response at 857 nm (Supporting Information, Figure S8), similar to previous results.[39] These findings indicate that (1) structural variation of multiscale particles can be reflected in different polarization-dependent optical responses, and (2) 3D structural changes at the ends of the particle can significantly alter LSP resonances. Hence, the optical properties of multiscale particles are very sensitive to nanoscale structural details.

CONCLUSIONS

In summary, multiscale Au particles with different ARs were fabricated, and the polarization-dependent scattering was measured. Variation in the length of the particles along the long axis resulted in the excitation of a single multipolar longitudinal mode and two distinct transverse modes with different multipolar orders. The measured LSP resonances were identified by the calculated FDTD scattering spectra, which allowed correlation of the resonance with specific structural features of the 3D, anisotropic particle. The calculated electric field intensity maps were used to determine the multipolar order of the plasmon resonances. Both far-field and near-field optical calculations indicated that structural asymmetry of 3D anisotropic NP leads to two different transverse modes, whereas the single longitudinal mode was determined by the elongated structure of multiscale particle. Our results suggest that multipolar plasmon resonances can be tuned over a wide spectral range by changing the structural parameters of the particles. In addition, our fabrication strategy offers the potential that LSP resonances can be easily tailored by

manipulating thickness and materials of NPs. The fabricated nanostructures can be adapted for different applications such as nonlinear optics, sensing, and optical imaging.

METHODS

Fabrication of Multiscale Au Particles. A soft interference lithography-line photomask was used to change AR of the patterned PR feature (Shipley 1805, thickness $t = 100$ nm) and ϕ was 90°, 45°, 44°, 42°, 28°, 20°, and 17° for AR = 1.0, 2.5, 2.6, 2.8, 3.4, 6.0 and 7.7, respectively. The feature sizes were first determined by the UV exposure dose and the developing condition which can be altered by the developing time and the dilution ratio of 351 Microposit developer with deionized (DI) water. Then, the feature sizes of PR were further tailored by reactive ion etching (RIE) using O_2 gas. RIE was employed to remove unwanted PR residues on the surface and to decrease the feature size width to ~120 nm. After deposition of 15 nm Cr using an electron beam evaporator, the Cr-deposited PR was lifted-off by sonicating the pattern in Microposit Remover 1165 for 5−10 min.

The Si (100) substrate was anisotropically etched in KOH/isopropyl alcohol (IPA) solution in which 33 mL of IPA was added to aqueous KOH solution (23−33 g of KOH/100 mL of DI water) at 72 °C on hot plate while stirring using a magnetic stirrer. The etching time was varied from 30 to 90 s depending on AR and desired type of particles (*i.e.*, Type A or B). The anisotropically etched Si was checked by LEO1525 field emission SEM. Then, 20 nm thick Au was deposited on the etched Si template using an electron beam evaporator. After the Cr/Au film in Cr etchant 1020 (Transene Corp., Danvers, MA) was removed, multiscale Au particles were released in dilute KOH solution (~10 mg/mL (KOH/DI water)) by etching Si under sonication for ≥1 h. After KOH was purified, the particles were released in DI water before use.

Measurement of Single Particle Scattering. Multiscale NPs were dispersed on indium tin oxide (ITO)-coated glass substrates patterned with Au alignment markers. The particles were identified by SEM to correlate the specific particle to the DF scattering spectra. Single particle immersed in oil ($n = 1.525$) was illuminated by broadband white light source (100 W, halogen lamp) through a polarizer that is mounted on a DF condenser in an inverted optical microscope (Nikon TE-2000U). The scattered light from the particle was collected by a 100X variable NA objective (NA = 0.5−1.3) and received by a spectrometer equipped with a liquid N_2-cooled CCD (Princeton instrument). The NA of the objective lens was set to 0.5 for measurement of single particle and background with particle and 1.3 for lamp profile. Spectra were taken from single particle, background without particle, and lamp profile under polarized light. The data were processed by subtracting background spectra from single particle spectra and then dividing it by lamp profile.

FDTD Calculations. FDTD simulations using commercial software (FDTD solution, Lumerical Inc. Vancouver, Canada) was employed to calculate the single particle scattering spectra, the distribution maps of electric field intensity and the real part of electric fields. Single particle scattering spectra were calculated using total-field scattered-field (TFSF) source that allows only scattered field to the detector. After identifying λ_1, λ_2, and λ_3, in single particle scattering spectra, the distribution of $|\mathbf{E}|^2$ and Re($\mathbf{E}$) were simulated using a plane wave source at each resonance. The optical constants of Au were taken from CRC in the spectrum range from 400 to 7000 nm.[54] All the calculations were performed in a homogeneous dielectric medium ($n = 1.525$). A uniform mesh size of 4 nm and perfectly matched layer boundary conditions were applied to x-, y-, and z-directions for all the simulations.

Conflict of Interest: The authors declare no competing financial interest.

Supporting Information Available: Measured scattering spectra under longitudinal polarization; calculated scattering spectra at different excitation directions; calculated scattering spectra showing dipole mode and higher modes for different AR particles; extinction spectra showing dipolar resonances in the particle array; calculated scattering spectra in the measured spectral range for the particles with different ARs; electric field intensity distributions exhibiting different multipolar orders of longitudinal and transverse modes for different AR particles; calculated scattering spectra for the particle with structural change at the ends; polar plots for nanopyramid. This material is available free of charge *via* the Internet at http://pubs.acs.org.

REFERENCES AND NOTES

1. Kreibig, U., Vollmer, M. *Optical Properties of Metal Clusters*; 1st ed.; Springer: New York, 1995.
2. El-Sayed, M. A.; Link, S. Spectral Properties and Relaxation Dynamics of Surface Plasmon Electronic Oscillations in Gold and Silver Nanodots and Nanorods. *J. Phys. Chem. B* **1999**, *103*, 8410–8426.
3. Schatz, G. C.; Kelly, K. L.; Coronado, E.; Zhao, L. L. The Optical Properties of Metal Nanoparticles: The Influence of Size, Shape, and Dielectric Environment. *J Phys. Chem. B* **2003**, *107*, 668–677.
4. Fendler, J. H.; Hutter, E. Exploitation of Localized Surface Plasmon Resonance. *Adv. Mater.* **2004**, *16*, 1685–1706.
5. Shuford, K. L.; Lee, J.; Odom, T. W.; Schatz, G. C. Optical Properties of Gold Pyramidal Shells. *J. Phys. Chem. C* **2008**, *112*, 6662–6666.
6. Maier, S. A. *Plasmonics: Fundamentals and Applications*; Springer: New York, 2007.
7. Khlebtsov, B. N.; Melnikov, A.; Khlebtsov, N. G. On the Extinction Multipole Plasmons in Gold Nanorods. *J. Quant. Spectrosc. Radiat.* **2007**, *107*, 306–314.
8. Bohren, C. F.; Huffman, D. R. *Absorption and Scattering of Light by Small Particles*; Wiley: New York, 1983.
9. Wei, H.; Reyes-Coronado, A.; Nordlander, P.; Aizpurua, J.; Xu, H. X. Multipolar Plasmon Resonances in Individual Ag Nanorice. *ACS Nano* **2010**, *4*, 2649–2654.
10. Yguerabide, J.; Yguerabide, E. E. Light-scattering Submicroscopic Particles as Highly Fluorescent Analogs and Their Use as Tracer Labels in Clinical and Biological Applications—I. Theory. *Anal. Biochem.* **1998**, *262*, 137–156.
11. Payne, E. K.; Shuford, K. L.; Park, S.; Schatz, G. C.; Mirkin, C. A. Multipole Plasmon Resonances in Gold Nanorods. *J. Phys. Chem. B* **2006**, *110*, 2150–2154.
12. Kreibig, U.; Schmitz, B.; Breuer, H. D. Separation of Plasmon-Polariton Modes of Small Metal Particles. *Phys. Rev. B* **1987**, *36*, 5027–5030.
13. Felidj, N.; Grand, J.; Laurent, G.; Aubard, J.; Levi, G.; Hohenau, A.; Galler, N.; Aussenegg, F. R.; Krenn, J. R. Multipolar Surface Plasmon Peaks on Gold Nanotriangles. *J. Chem. Phys.* **2008**, *128*, 094702/1–094702/5.
14. Encina, E. R.; Coronado, E. A. Plasmonic Nanoantennas: Angular Scattering Properties of Multipole Resonances in

Noble Metal Nanorods. *J. Phys. Chem. C* **2008**, *112*, 9586–9594.

15. Laurent, G.; Felidj, N.; Aubard, J.; Levi, G.; Krenn, J. R.; Hohenau, A.; Schider, G.; Leitner, A.; Aussenegg, F. R. Evidence of Multipolar Excitations in Surface Enhanced Raman Scattering. *Phys. Rev. B* **2005**, *71*, 045430/1–045430/6.

16. Laurent, G.; Felidj, N.; Aubard, J.; Levi, G.; Krenn, J. R.; Hohenau, A.; Schider, G.; Leitner, A.; Aussenegg, F. R. Surface Enhanced Raman Scattering Arising from Multipolar Plasmon Excitation. *J. Chem. Phys.* **2005**, *122*, 011102/1–011102/4.

17. Billot, L.; de la Chapelle, M. L.; Grimault, A. S.; Vial, A.; Barchiesi, D.; Bijeon, J. L.; Adam, P. M.; Royer, P. Surface Enhanced Raman Scattering on Gold Nanowire Arrays: Evidence of Strong Multipolar Surface Plasmon Resonance Enhancement. *Chem. Phys. Lett.* **2006**, *422*, 303–307.

18. Russier-Antoine, I.; Benichou, E.; Bachelier, G.; Jonin, C.; Brevet, P. F. Multipolar Contributions of the Second Harmonic Generation from Silver and Gold Nanoparticles. *J. Phys. Chem. C* **2007**, *111*, 9044–9048.

19. Oldenburg, S. J.; Hale, G. D.; Jackson, J. B.; Halas, N. J. Light Scattering from Dipole and Quadrupole Nanoshell Antennas. *Appl. Phys. Lett.* **1999**, *75*, 1063–1065.

20. Shuford, K. L.; Ratner, M. A.; Schatz, G. C. Multipolar Excitation in Triangular Nanoprisms. *J. Chem. Phys.* **2005**, *123*, 114713/1–114713/9.

21. Rang, M.; Jones, A. C.; Zhou, F.; Li, Z. Y.; Wiley, B. J.; Xia, Y. N.; Raschke, M. B. Optical Near-Field Mapping of Plasmonic Nanoprisms. *Nano Lett* **2008**, *8*, 3357–3363.

22. Bukasov, R.; Shumaker-Parry, J. S. Highly Tunable Infrared Extinction Properties of Gold Nanocrescents. *Nano Lett.* **2007**, *7*, 1113–1118.

23. Rochholz, H.; Bocchio, N.; Kreiter, M. Tuning Resonances on Crescent-Shaped Noble-Metal Nanoparticles. *New J. Phys.* **2007**, *9*, 53.

24. Kumbhar, A. S.; Kinnan, M. K.; Chumanov, G. Multipole Plasmon Resonances of Submicron Silver Particles. *J. Am. Chem. Soc.* **2005**, *127*, 12444–12445.

25. Wang, H.; Halas, N. J. Mesoscopic Au "Meatball" Particles. *Adv. Mater.* **2008**, *20*, 820–825.

26. Oldenburg, S. J.; Jackson, J. B.; Westcott, S. L.; Halas, N. J. Infrared Extinction Properties of Gold Nanoshells. *Appl. Phys. Lett.* **1999**, *75*, 2897–2899.

27. Slaughter, L. S.; Chang, W. S.; Swanglap, P.; Tcherniak, A.; Khanal, B. P.; Zubarev, E. R.; Link, S. Single-Particle Spectroscopy of Gold Nanorods beyond the Quasi-Static Limit: Varying the Width at Constant Aspect Ratio. *J. Phys. Chem. C* **2010**, *114*, 4934–4938.

28. Krenn, J. R.; Schider, G.; Rechberger, W.; Lamprecht, B.; Leitner, A.; Aussenegg, F. R.; Weeber, J. C. Design of Multipolar Plasmon Excitations in Silver Nanoparticles. *Appl. Phys. Lett.* **2000**, *77*, 3379–3381.

29. Henzie, J.; Shuford, K. L.; Kwak, E. S.; Schatz, G. C.; Odom, T. W. Manipulating the Optical Properties of Pyramidal Nanoparticle Arrays. *J. Phys. Chem. B* **2006**, *110*, 14028–14031.

30. Lee, J.; Hasan, W.; Odomt, T. W. Tuning the Thickness and Orientation of Single Au Pyramids for Improved Refractive Index Sensitivities. *J. Phys. Chem. C* **2009**, *113*, 2205–2207.

31. Sweeney, C. M.; Stender, C. L.; Nehl, C. L.; Hasan, W.; Shuford, K. L.; Odom, T. W. Optical Properties of Tipless Gold Nanopyramids. *Small* **2011**, *7*, 2032–2036.

32. Sonnichsen, C.; Schubert, O.; Becker, J.; Carbone, L.; Khalavka, Y.; Provalska, T.; Zins, I. Mapping the Polarization Pattern of Plasmon Modes Reveals Nanoparticle Symmetry. *Nano Lett.* **2008**, *8*, 2345–2350.

33. Muskens, O. L.; Bachelier, G.; Del Fatti, N.; Vallee, F.; Brioude, A.; Jiang, X. C.; Pileni, M. P. Quantitative Absorption Spectroscopy of a Single Gold Nanorod. *J. Phys. Chem. C* **2008**, *112*, 8917–8921.

34. Nehl, C. L.; Liao, H. W.; Hafner, J. H. Optical Properties of Star-Shaped Gold Nanoparticles. *Nano Lett.* **2006**, *6*, 683–688.

35. Lee, K. S.; El-Sayed, M. A. Dependence of the Enhanced Optical Scattering Efficiency Relative to That of Absorption for Gold Metal Nanorods on Aspect Ratio, Size, End-Cap Shape, and Medium Refractive Index. *J. Phys. Chem. B* **2005**, *109*, 20331–20338.

36. Canfield, B. K.; Kujala, S.; Kauranen, M.; Jefimovs, K.; Vallius, T.; Turunen, J. Remarkable Polarization Sensitivity of Gold Nanoparticle Arrays. *Appl. Phys. Lett.* **2005**, *86*, 183109/1–183109/3.

37. Hicks, E. M.; Zou, S. L.; Schatz, G. C.; Spears, K. G.; Van Duyne, R. P.; Gunnarsson, L.; Rindzevicius, T.; Kasemo, B.; Kall, M. Controlling Plasmon Line Shapes through Diffractive Coupling in Linear Arrays of Cylindrical Nanoparticles Fabricated by Electron Beam Lithography. *Nano Lett.* **2005**, *5*, 1065–1070.

38. Odom, T. W.; Henzie, J.; Kwak, E. S. Mesoscale Metallic Pyramids with Nanoscale Tips. *Nano Lett.* **2005**, *5*, 1199–1202.

39. Lee, J.; Hasan, W.; Stender, C. L.; Odom, T. W. Pyramids: A Platform for Designing Multifunctional Plasmonic Particles. *Acc. Chem. Res.* **2008**, *41*, 1762–1771.

40. Zhou, W.; Gao, H. W.; Odom, T. W. Toward Broadband Plasmonics: Tuning Dispersion in Rhombic Plasmonic Crystals. *ACS Nano* **2010**, *4*, 1241–1247.

41. Stefani, F. D.; Dondapati, S. K.; Sau, T. K.; Hrelescu, C.; Klar, T. A.; Feldmann, J. Label-free Biosensing Based on Single Gold Nanostars as Plasmonic Transducers. *Acs Nano* **2010**, *4*, 6318–6322.

42. Chen, S. H.; Carroll, D. L. Synthesis and Characterization of Truncated Triangular Silver Nanoplates. *Nano Lett.* **2002**, *2*, 1003–1007.

43. Sonnichsen, C.; Franzl, T.; Wilk, T.; von Plessen, G.; Feldmann, J.; Wilson, O.; Mulvaney, P. Drastic Reduction of Plasmon Damping in Gold Nanorods. *Phys. Rev. Lett.* **2002**, *88*, 077402/1–077402/4.

44. Cao, L.; Nome, R. A.; Montgomery, J. M.; Gray, S. K.; Scherer, N. F. Controlling Plasmonic Wave Packets in Silver Nanowires. *Nano Lett.* **2010**, *10*, 3389–3394.

45. Anderson, L. J. E.; Payne, C. M.; Zhen, Y. R.; Nordlander, P.; Hafner, J. H. A Tunable Plasmon Resonance in Gold Nanobelts. *Nano Lett.* **2011**, *11*, 5034–5037.

46. Liu, M. Z.; Lee, T. W.; Gray, S. K.; Guyot-Sionnest, P.; Pelton, M. Excitation of Dark Plasmons in Metal Nanoparticles by a Localized Emitter. *Phys. Rev. Lett.* **2009**, *102*, 107401/1–107401/4.

47. Ekinci, Y.; Christ, A.; Agio, M.; Martin, O. J. F.; Solak, H. H.; Loffler, J. F. Electric and Magnetic Resonances in Arrays of Coupled Gold Nanoparticle In-tandem Pairs. *Opt. Express* **2008**, *16*, 13287–13295.

48. Encina, E. R.; Coronado, E. A. Resonance Conditions for Multipole Plasmon Excitations in Noble Metal Nanorods. *J. Phys. Chem. C* **2007**, *111*, 16796–16801.

49. Encina, E. R.; Perassi, E. A.; Coronado, E. A. Near-Field Enhancement of Multipole Plasmon Resonances in Ag and Au Nanowires. *J. Phys. Chem. A* **2009**, *113*, 4489–4497.

50. Novotny, L. Effective Wavelength Scaling for Optical Antennas. *Phys. Rev. Lett.* **2007**, *98*, 266802/1–266802/4.

51. Jackson, J. D. *Classical Electrodynamics*, 2 ed.; Wiley: New York, 1975.

52. Schider, G.; Krenn, J. R.; Hohenau, A.; Ditlbacher, H.; Leitner, A.; Aussenegg, F. R.; Schaich, W. L.; Puscasu, I.; Monacelli, B.; Boreman, G. Plasmon Dispersion Relation of Au and Ag Nanowires. *Phys. Rev. B* **2003**, *68*, 155427/1–155427/4.

53. Ross, B. M.; Lee, L. P. Comparison of Near- and Far-Field Measures for Plasmon Resonance of Metallic Nanoparticles. *Opt. Lett.* **2009**, *34*, 896–898.

54. Lide, D. R. *Handbook of Chemistry and Physics*, 85 ed.; CRC Press: Boca Raton, FL, **2004**.